# Face-to-face annealed sputtered $BaSi_2$: Investigations on surface homogeneity, film properties, and annealing mechanisms

Yilei Tian,* Miro Zeman, and Olindo Isabella†
*Photovoltaic Materials and Devices Group, Delft University of Technology, Delft 2628 CD, Netherlands*

(Received 2 August 2020; accepted 11 December 2020; published 29 December 2020)

Regarded as a promising candidate for absorber material in photovoltaic applications, $BaSi_2$ confronts the challenge of high-quality material synthesis via low-cost processes. Here, we fabricated $BaSi_2$ thin films through the industrially applicable sputtering technique with the face-to-face annealing (FTFA) approach. The employment of the FTFA approach leads to an improvement of the sputtered $BaSi_2$ from perspectives of surface homogeneity and crystal quality. Various covers are applied in the FTFA, including $BaSi_2$, glass, and Si, which causes alterations in the film's electrical and optical properties. These impacts of the FTFA method on sputtered $BaSi_2$ films stem from two aspects, i.e., heat redistributions caused by the variation of thermal networks, and interfacial interactions within the confined space between the cover and the film. The FTFA approach provides a facile strategy for minimizing the impacts of $BaSi_2$ surface oxidation during high-temperature processes. These results and findings can push forward the material development of $BaSi_2$ and its photovoltaic applications.

DOI: 10.1103/PhysRevMaterials.4.125403

## I. INTRODUCTION

Possessing a band gap $E_g = \sim 1.3$ eV, and a high absorption coefficient ($\alpha$) over $10^4\,cm^{-1}$ at the photon energy of 1.5 eV, which is much larger than that of Si and is comparable to that of commercialized materials such as copper indium gallium selenide (CIGS), $BaSi_2$ exhibits great potential and promise in photovoltaic solar cell applications [1–3]. Besides, its inherent advantages of nontoxicity, adequate elemental availability, and excellent electrical properties (long minority-carrier lifetime $t \sim 10\,\mu s$ and diffusion length $L \sim 10\,\mu m$, high carrier mobility $\mu \sim 816\,cm^2\,V^{-1}\,s^{-1}$, etc.) facilitate the realization of low-cost and highly efficient $BaSi_2$-based thin-film solar cells [4–6]. Various techniques have been employed in the synthesis of $BaSi_2$ thin films, such as molecular beam epitaxy (MBE), thermal evaporation (TE), pulsed laser deposition (PLD), and sputtering [7–12]. Among them, sputtering is regarded as an industry applicable technique enabling low-cost magnification of $BaSi_2$ films on various substrates.

Theoretically, the conversion efficiency ($\eta$) of an $n$-$p$ $BaSi_2$ homojunction solar cell can reach 22.5%–25%, while $BaSi_2$/Si and $n$-Si/$BaSi_2$/$p$-Si heterojunction solar cells possess potential $\eta$ up to 22.7% and 30.4%, respectively [13–15]. However, the highest experimentally obtained was achieved by a $p$-$BaSi_2$/$n$-Si heterojunction solar cell with $\eta = 10\%$, wherein it was an $n$-Si wafer rather than $p$-$BaSi_2$ acting as the light absorber [16]. The $n^+$-$BaSi_2$/$p$-$BaSi_2$/$p^+$-$BaSi_2$ diode only exhibited an extremely low $\eta$ of ~0.1%, which is caused by a high volume of defects within the $BaSi_2$ [17]. Defects within the $BaSi_2$ can originate either from thin-film depositions, for instance, synthesis techniques, conditions, source materials, etc., or from postgrowth treatments, such as doping, subsequent depositions, etc. [18–23]. The postdeposition annealing was always employed to reduce the content of defects [18,21,23]. Besides, annealing treatment was used to enable the crystallization of amorphous $BaSi_2$, for instance, room-temperature deposited samples and ion-implantation doped $BaSi_2$ films [20,21,24].

However, the employment of high-temperature annealing, in turn, can induce other issues such as surface oxidation and induced atomic interdiffusions [19,20], which play a rather significant role in the quality control of sputtered $BaSi_2$ films. The annealing process is essential for the crystallization of room-temperature sputtered film. As a consequence of surface oxidation, an inhomogeneous surface of annealed samples can always be observed, which consists of high-volume and nonuniformly distributed impurities such as BaO, Si nanocrystals (NCs), amorphous Si ($a$-Si), $FeSi_2$, $BaCO_3$, etc. [20,25,26]. Vacuum annealing conditions have been applied to suppress surface oxidation [25], which only made a limited contribution to the alleviation of surface oxidation. Additionally, $a$-Si antioxidation layers were deposited on the $BaSi_2$ surface before the annealing, in which a thick $a$-Si layer around 50 nm was needed to effectively suppress surface oxidation [26]. The thick antioxidation layer would be retained at the film surface in the form of a multiphase Si ($a$-Si and Si NCs) layer, introducing additional issues into the sputtered $BaSi_2$ film applications. Obtaining a film surface with fewer impurities and defects caused by oxidation and diffusion during annealing is crucial for the development of sputtered $BaSi_2$.

A face-to-face annealing (FTFA) approach is frequently used for GaAs semiconductors to prevent the outdiffusion of arsenic, in which the GaAs wafer is placed between a bottom Si wafer and a top GaAs wafer during the annealing [27]. Besides, the FTFA approach has been applied to suppress

*y.tian@tudelft.nl
†o.isabella@tudelft.nl

 

surface oxidation of thin-film materials, such as ZnO, AlN, $Ga_2O_3$, etc. [28–30]. As compared to the conventional annealing method, in which the film surface is exposed to the annealing ambient, the FTFA approach improves the thin-film properties due to a confined surface condition of the films and complicated solid-phase reactions [27]. A similar method has also been employed in evaporated $BaSi_2$ films, in which the FTFA method was applied to suppress the film surface oxidation for the sake of understanding the postannealing effects on film property improvement [31,32]. Nevertheless, the effects of the FTFA method on the properties of $BaSi_2$ and its underlying mechanism have not yet been systematically studied.

Herein, amorphous $BaSi_2$ thin films were deposited on glass substrates by radio-frequency magnetron sputtering and were crystallized by applying the FTFA approach. The employment of the FTFA approach drastically enhances the sputtered $BaSi_2$ film surface homogeneity in terms of structure and composition. Applying various FTFA cover materials demonstrates the potential of controlling the electrical and optical properties of $BaSi_2$. The mechanism of the FTFA approach is discussed from thermodynamic views on heat transfer and chemical physics perspectives of interfacial interactions. These results and findings shed light on the application and optimization of the FTFA for $BaSi_2$ film fabrications and offer contributions to the development of the $BaSi_2$ material improvement methods.

## II. EXPERIMENT

*Depositions.* $BaSi_2$ films were deposited by radio-frequency (RF) magnetron sputtering equipment (Kurt J. Lesker) using a stoichiometric ceramic $BaSi_2$ target. Corning Eagle XG glass was used as substrates. Ar was used for sputtering. Before the deposition, the target was presputtered for cleaning. The plasma power density and deposition pressure were set as $0.617\,W/cm^2$ and 1 Pa, respectively. Depositions were carried out at room temperature. The thickness of $BaSi_2$ was kept at around 500 nm. The subsequent annealing processes were carried out in a high-vacuum (HV) environment ($<10^{-4}$ Pa) with a temperature of 600 °C. The annealing duration was 30 min.

*Characterizations*. Surface topology was analyzed by a three-dimensional (3D) laser scanning microscope (Keyence VK-X250). Raman spectroscopy analysis was carried out on a Renishaw inVia Raman microscope with 633-nm laser excitation. Raman mapping was executed with a scan area of $40 \times 40\,\mu m^2$. The acquisition time per scan was 10 s. For single spectrum collections, the acquisition time was set as 100 s. Raman spectra were fitted with Renishaw WiRE by using broadened Gaussian/Lorentzian line shapes. Raman maps and peak information were acquired from fitted results. The majority carrier type and concentration were determined through resistivity and Hall effect measurements with van der Pauw geometry. Al contacts were deposited by vacuum thermal evaporation (PRO500S, Provac), and were subsequently annealed at 130 °C for 30 min to ensure Ohmic contact. Wavelength-dependent reflectance and transmittance were obtained on a PerkinElmer Lambda 1050 UV-Vis-NIR spectrometer. Absorptance was calculated by absorptance (%) = 100% − reflectance (%) – transmittance (%).

## III. RESULTS AND DISCUSSION

### A. FTFA approach and effects on surface homogeneity

The FTFA approach is illustrated in Fig. 1(a), in which two $BaSi_2$ films on the glass substrate ($BaSi_2$/glass) are placed together, the film surface to the film surface. The upper one functions as the cover for the FTFA approach, while the lower one is the obtained sample. The FTFA sample shows a metallic-gray appearance different from the blackish-blue surface of the conventionally annealed sample (exposed to the vacuum annealing ambient), as displayed by Figs. 1(b) and 1(c). The tiny blackish-blue area indicated in Fig. 1(b) is the result of the partially overlapped FTFA as illustrated in Fig. 1(d).

The optical microscopy image of the boundary region between the covered (blackish-blue) and the exposed (metallic-gray) areas is shown in Fig. 1(e). There is a clear transition from a heterogeneous surface in the exposed area to a quite homogeneous surface in the covered area. As shown in Fig. 1(e), the exposed area shows a nonuniform surface, where two distinct regions are observed. This surface heterogeneity in the exposed area can be ascribed to the surface oxidation of $BaSi_2$ due to the residual oxidants in the annealing ambient [20]. An enhancement in surface homogeneity is clearly shown in the covered area. The variation of surface appearance is normally related to its composition or geometry.

Figure 1(f) shows the reconstructed 3D image of the boundary region. In fact, the exposed area and the covered area demonstrate quite a smooth surface with a similar height. This suggests that the differences in surface appearance and homogeneity are likely stimulated by the composition variation rather than the geometrical change. Meanwhile, we can notice a rougher surface of the transition area between the exposed and covered areas. The transition region contains randomly distributed hills with heights of tens to hundreds of nanometers. This likely results from the lateral elemental diffusion between exposed and covered areas. The surface oxidation occurring at the exposed area can lead to an atomic movement from the covered area to the oxidation sites. Such atomic movements can lead to mass accumulations in the transition region and formations of those hills.

To understand the link between the variation of surface-appearance homogeneity with the film composition, Raman mapping measurements are carried out at the area indicated by the dashed-line box Fig. 1(e). Besides the strongest $A_g$ peak of $BaSi_2$ located at $\sim 486\,cm^{-1}$, maps of the often-observed impurities $FeSi_2$ and Si nanocrystals (NCs) of sputtered $BaSi_2$ films with the Raman peaks at $\sim 247$ and $\sim 519\,cm^{-1}$, respectively, are profiled in Fig. 2 [33–36]. Figures 2(a)–2(c) show the Raman peak-intensity maps of $FeSi_2$, Si NCs, and the $A_g$ peak of $BaSi_2$, respectively. The peak-intensity maps can indicate the phase-content distribution within the detected depth of the film surface that is around 100–200 nm for $BaSi_2$ films [20]. Indeed, their Raman maps demonstrate three areas with different phase-distribution patterns, i.e., (i) $X < -5\,\mu m$, (ii) $-5\,\mu m < X < 10\,\mu m$, and (iii) $X > 10\,\mu m$. These areas precisely correspond to (i) the exposed area, (ii) the transition area, and (iii) the covered area in Fig. 1(e), respectively.

In the exposed area ($X < -5\,\mu m$), Raman peak-intensity images demonstrate the phase distributions in good agreement

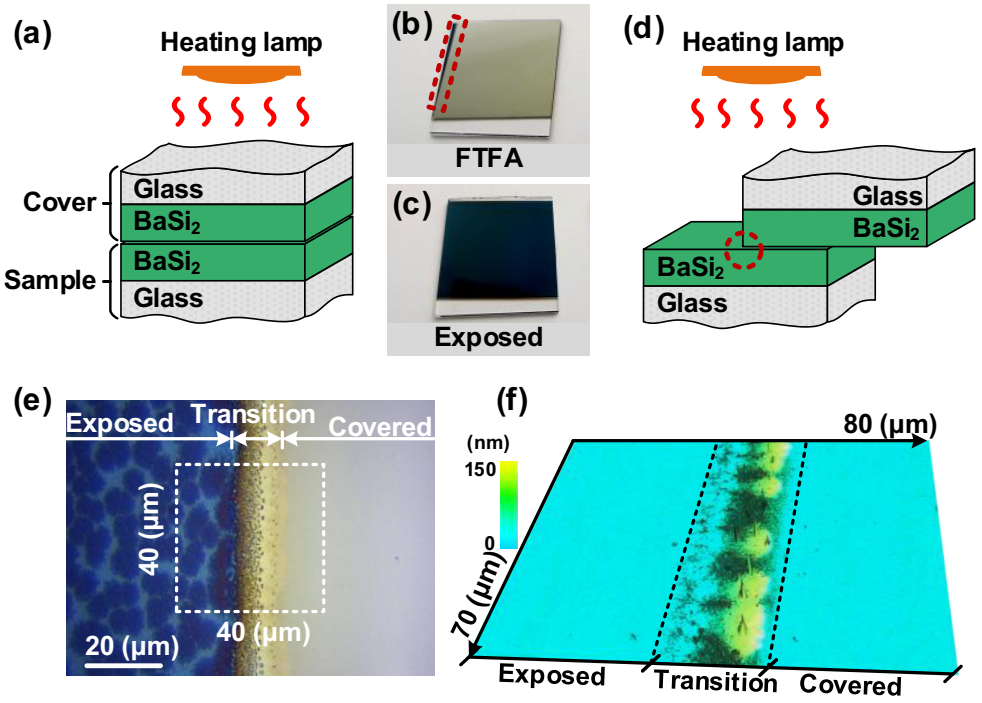


FIG. 1. Schematic illustrations of (a) fully and (d) partially overlapped FTFA configurations for $BaSi_2$ annealing. Photographs of $BaSi_2$ samples (b) annealed by FTFA methods, and (c) exposed to annealing ambient. (e) Optical and (f) 3D-laser micrographs of the red-dashed boundary region between the exposed and covered areas in (b).

with the optical micrograph color pattern in Fig. 1(e). Although all compositions show inhomogeneous distributions, we can notice that the distribution of Si NCs is the reverse of those of $FeSi_2$ and $BaSi_2$ in the exposed area. This is understandable considering that Si NCs are formed as the outcome of $BaSi_2$ oxidation and induced atomic diffusions within the films [18,20,37,38]. The source of $FeSi_2$ can be ascribed to the impurities from the sputtering target [26], and it thus shows a similar distribution to that of $BaSi_2$.

A dramatic change in compositions can be noticed in the transition area. Limited sites at the transition area show the Raman trace of $FeSi_2$, and we can observe the sudden drop of $FeSi_2$ peak intensity at the boundary between the covered and transition area ($X \sim -5\,\mu$m). Differently, Si NCs show an increase of peak intensity when approaching the transition area, which reaches the maximum near the boundary between the exposed and transition areas ($-8\,\mu\text{m} < X < -2\,\mu\text{m}$), and it then decreases gradually when $X > -2\,\mu$m. Meanwhile, some sites near the boundary of transition and covered areas show an abnormally high Si NC Raman signal, for instance, points (8,0) and (8,10) indicated in Fig. 2(b), which may correspond to hills observed in Fig. 1(f). The peak-intensity profile of $BaSi_2$ ($A_g$) shows a similar trend to that of Si NCs at the exposed/transition boundary region, while it shows an intensity dip in the middle of the transition area. It is noteworthy that $BaSi_2$ ($A_g$) peak intensities show similar values at two boundary regions, i.e., the exposed/transition and the transition/covered boundaries.

When it goes to the covered area, the signal of $FeSi_2$ and Si NCs can no longer be collected. Only the $BaSi_2$ ($A_g$) is detected, which shows a relatively homogeneous peak-intensity distribution. We may speculate that the FTFA approach can alleviate the formation/crystallization of $FeSi_2$ and Si NCs within the $BaSi_2$ film. However, the $BaSi_2$ ($A_g$) peak intensity at the covered area is much lower than that at the exposed area. Although this can imply a lower $BaSi_2$ content at the covered area within the detected depth, we cannot yet assert that the FTFA method reduces the concentration of $BaSi_2$ at the dimension of the entire thickness, considering that the surface compositional and structural difference between these two areas may alter the Raman-laser penetration depth, leading to the peak-intensity variations.

The full width at half maximum (FWHM) of the $A_g$ peak is further extracted as an indicator for $BaSi_2$ crystal quality, and its mapping result is profiled in Fig. 2(d). An improvement of $BaSi_2$ crystal quality at the covered area is suggested by the decrease of FWHM values, though this area shows a lower $BaSi_2$ ($A_g$) peak intensity. The suppression of the impurity formations may keep the stoichiometry between Ba and Si within the sputtered films, and then results in better $BaSi_2$ crystal quality.

Based on these Raman mapping results together with microscopic results shown in Fig. 1, we can deduce that the FTFA approach effectively improves the surface compositional homogeneity of $BaSi_2$ by suppressing the impurity formations, which also leads to a better $BaSi_2$ crystal quality, as compared to the conventional annealing method.

### B. Influence of FTFA cover materials

Besides the $BaSi_2$/glass cover, other covers including glass and silicon wafer are also employed for FTFA. These FTFA-annealed samples with covers of $BaSi_2$/glass, glass, and silicon wafer, herein denoted as $BaSi_2$-B, $BaSi_2$-G,

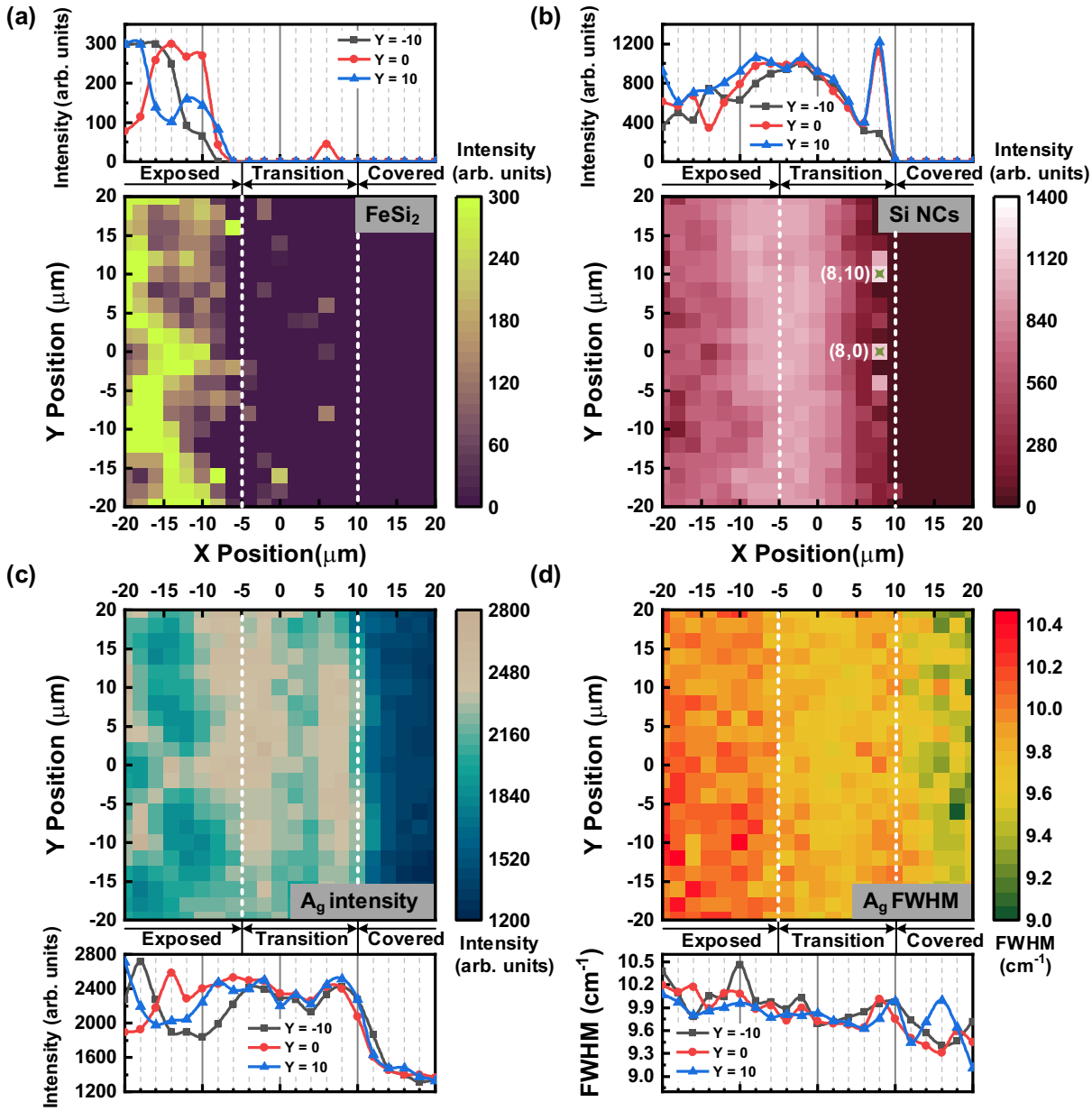


FIG. 2. Raman peak-intensity maps and horizontal profiles ($Y = -10$, 0, and 10 $\mu$m) of (a) $FeSi_2$ (~247 $cm^{-1}$), (b) Si NCs (~519 $cm^{-1}$), and (c) $BaSi_2$ ($A_g$) (~486 $cm^{-1}$). (d) FWHM distribution of $BaSi_2$ ($A_g$) ($A_g$) peak and its horizontal profiles.

and $BaSi_2$-S, respectively, as expected, demonstrate homogeneous surfaces, while the sample exposed to annealing ambient (named $BaSi_2$-E) exhibits a nonuniform surface including two distinct regions, i.e., dark grain and light bright filling regions, as shown in Fig. S1 in the Supplemental Material [39]. Their Raman spectra are presented in Fig. 3(a). In good agreement with Raman mapping results, the dark grain area of $BaSi_2$-E exhibits an obvious $FeSi_2$ peak with a weak Si NCs peak, while the bright filling area demonstrates stronger Si NCs without the $FeSi_2$ peak. On the contrary, FTFA samples only present Raman peaks originating from the $BaSi_2$, regardless of the types of the cover.

Despite the same Raman spectral shapes of FTFA samples, it is worthwhile to address the slight peak-position shift among these samples. The Raman peak-position shift is normally related to defects within the $BaSi_2$ crystal. Herein, the $A_g$ peak position of $BaSi_2$ is taken for discussions. As compared to the calculated results ($A_g$ peak at 493 $cm^{-1}$), all samples display a blueshift (toward lower wave number), which is caused by the existence of defects, including Ba substituted for Si antisites ($Ba_{Si}$), Si vacancies ($V_{Si}$), and Si interstitials ($Si_i$) [27,40]. The larger wave number of the $A_g$ peak suggests a lower volume of these defects. All FTFA samples hold larger $A_g$ position wave numbers than that of $BaSi_2$-E, which implicates a diminution of the defect content owing to the FTFA method. Among them, $BaSi_2$-S exhibits the highest $A_g$ position wave number of 486.86 $cm^{-1}$, indicating its lower content of those above-mentioned de-

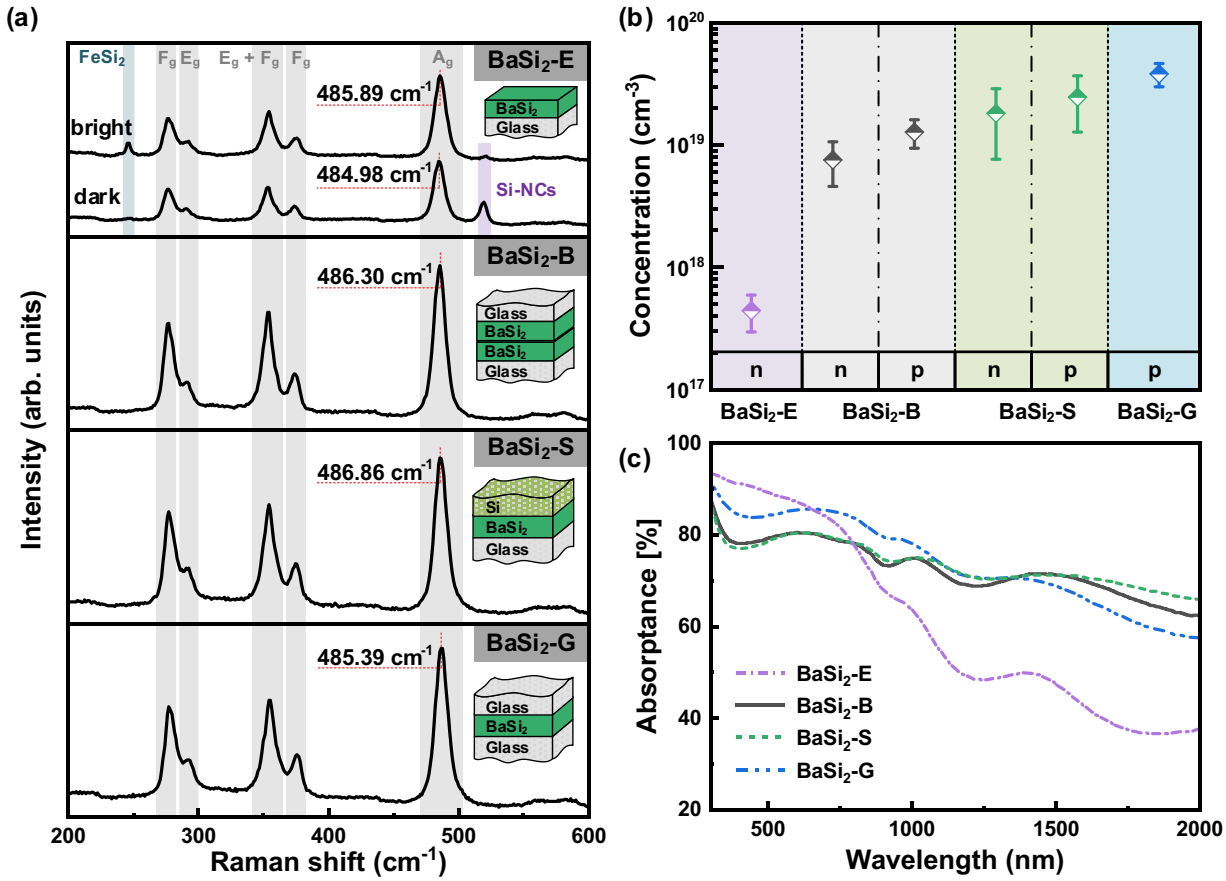


FIG. 3. (a) Raman spectra, (b) carrier concentrations, and (c) absorptance curves of $BaSi_2$-E, $BaSi_2$-B, $BaSi_2$-S, and $BaSi_2$-G.

fects. $BaSi_2$-B and $BaSi_2$-G possess slightly lower values of 486.30 and 485.39 $cm^{-1}$, respectively. Detailed Raman-peak information of sputtered $BaSi_2$ films, together with samples fabricated via other techniques, is summarized in Table S1 in the Supplemental Material [39].

Figure 3(b) shows the carrier concentrations of sputtered $BaSi_2$ film with different cover materials during the FTFA. A transition of conductivity type from *n* type to *p* type is observed. $BaSi_2$-E exhibits an *n*-type conductivity, while $BaSi_2$-G presents a *p*-type conductivity. During the repeated measurements of the majority carrier type, $BaSi_2$-B and $BaSi_2$-S randomly demonstrate *n*- or *p*-type conductivity with similar frequencies. We speculate comparable electron and hole concentrations of these samples. Besides the variation of conductivity type, an increase of the magnitude of carrier concentration, as well as a decrease of the film resistivity (see Fig. S2 in the Supplemental Material [39]), can be observed when applying the FTFA method. The FTFA samples exhibit carrier density on the scale of $10^{19}\,cm^{-3}$, which is much higher than that of $BaSi_2$-E ($\sim 4.5 \times 10^{17}\,cm^{-3}$).

Given that $BaSi_2$ films here are undoped, their *n*- and *p*-type conductivities can be attributed to the existence of $V_{Si}$'s that function as donors, and Ba vacancies ($V_{Ba}$) that behave as acceptors, respectively [17,31,41]. Indicated by the blueshift of Raman peaks, we can expect the reduction of $V_{Si}$ in the film after applying FTFA, and the conductivity transition can be regarded as a result of the reduction of $V_{Si}$ or donors. Meanwhile, the employment of FTFA may trigger the generation of other types of defects, such as $V_{Ba}$ defects. Together with the reduction of $V_{Si}$, they can lead to a *p*-type conductivity of $BaSi_2$-G. The increase of the magnitude of carrier density can be related to a high volume of metallic/defective phase within the film, which is indicated by their optical properties.

Their wavelength-dependent absorptance curves are shown in Fig. 3(c), derived from transmittance and reflectance curves in Fig. S3 in the Supplemental Material [39]. Although the FTFA approach can enhance $BaSi_2$ crystal quality, it does not significantly improve the $BaSi_2$ optical absorption properties. Conversely, we can notice that FTFA samples show a decrease of absorptance at the UV and visible wavelength window, and pretty high-absorptance tails at the near-infrared (NIR) wavelength range. Such optical property degrading is normally related to defective and/or metallic impurities/phases within the films, which may generate free carriers and cause the increase of carrier density as mentioned above.

### C. Mechanisms of the FTFA approach

The employment of the FTFA approach in the crystallization of sputtered $BaSi_2$ leads to significant surface homogeneity improvement as compared to the conventional annealing approach. The electrical and optical properties can be altered by applying various cover materials in the FTFA.

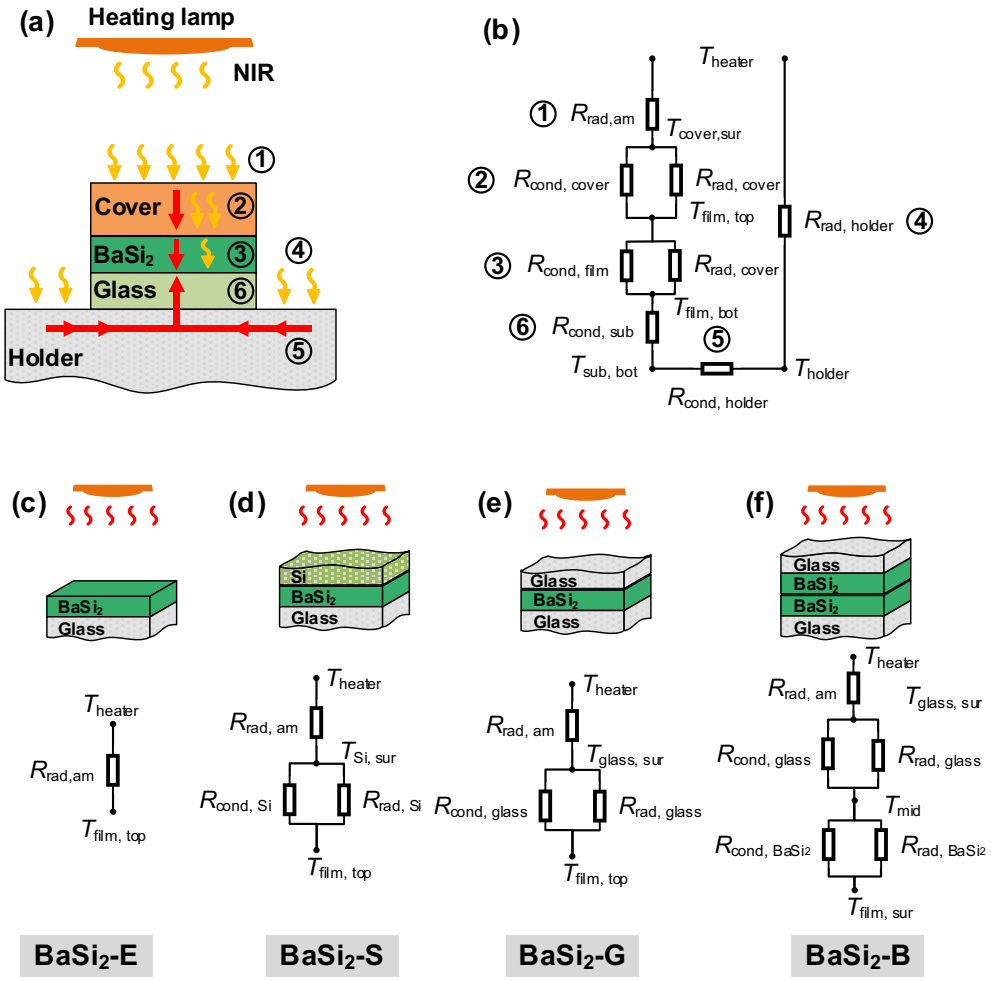


FIG. 4. (a) Schematic illustration of the heat transfer process in the FTFA sample and (b) the heat transfer thermal resistance network model (rad = radiation, am = ambient, sur = surface, cond = conduction, sub = substrate). Thermal resistance network of heat transfer from the heater to film surface in (c) $BaSi_2$-E, (d) $BaSi_2$-S, (e) $BaSi_2$-G, and (f) $BaSi_2$-B.

These effects of the FTFA method can be explained from considerations of heat transfer and surface reactions.

### *1. Heat transfer in the FTFA system*

Halogen heating lamps were applied for heating the sample through radiation, whose main emitting wavelength ranges from 1 to 1.6 $\mu$m (NIR). The introduction of additional cover material between the heat source and the sample would alter the heat transfer system and change the way the sample is heated. Figure 4(a) illustrates the heat transfer process during the FTFA. Heat flux can reach the sample by two routes, i.e., through the cover or the holder, as shown in Fig. 4(a), which can be described below.

Heat transfer through the cover**.**

Process 1: Radiative heat transfer from the heater to the cover surface.

Process 2: Absorption and transmission in the cover. The process of radiation traversing the medium (herein the cover) can be described by the radiative transfer equation (RTE) [42]. It is complicated to solve such a five-dimensional integro-differential equation. For simplicity, we only make a qualitative description of the process and ignore the scattering and emission processes. The absorption of the radiant flux can heat the cover and leads to heat transfer via conduction through the cover. Meanwhile, part of the radiant flux travels through the cover and reaches the sample surface.

Process 3: The behavior of radiant flux in the $BaSi_2$ film is similar to that in the cover. Thanks to the high absorption of the amorphous $BaSi_2$ at the IR and NIR window [20], radiant flux can be effectively absorbed within the $BaSi_2$ layer, enabling its crystallization.

Heat transfer through the holder.

Process 4: Radiative heat transfer from the heater to the titanium sample holder, effectively heating the holder.

Process 5: Conduction heat transfer within the holder.

Process 6: Conduction heat transfer through the glass substrate toward the film bottom.

The thermal resistance ($R_{th}$) network model of the whole process is illustrated in Fig. 4(b). The thermal resistance is defined by [43],

$$R_{th} = \Delta T/q, \tag{1}$$

where $\Delta T$ is the temperature difference, and $q$ is the heat flux passing through the resistance. The metal holder, being a good NIR radiant flux absorber, is rapidly heated up and the resulting heat is transferred to the film through the glass substrate. We may assume that the amount of heat transferred through the holder is similar among all samples, due to the same substrate and holder in all cases. We focus on the analysis of heat transfer from the heater to the film surface. i.e., Processes 1 and 2.

Figures 4(c)–4(f) show the thermal resistance network models of the heat transfer from the heater ($T_{\text{heater}}$) to the film top surface ($T_{\text{film,top}}$) in the exposed and FTFA samples. Radiative and conductive heat transfer mechanisms are involved, which can be described by radiative ($R_{\text{rad}}$) and conductive ($R_{\text{cond}}$) thermal resistance [43]. Given the high-vacuum ambient, the radiant flux can arrive at the sample surface with limited energy loss, which indicates a low thermal resistance of the ambient ($R_{\text{rad,am}}$). We can assume all samples share a similar and low $R_{\text{rad,am}}$.

In $BaSi_2$-E, the exposed amorphous $BaSi_2$ film directly absorbs the radiant flux. Note that the amorphous $BaSi_2$ presents a high absorption at the NIR window [20]. The absorption of radiant flux increases the temperature of the film. Together with the heat from the holder, it enables the crystallization of the film. The crystallization of $BaSi_2$ decreases its NIR absorption, letting the radiant flux propagate deeper into the layer and thus promoting its crystallization.

Placing the covers of silicon and glass does not substantially change the $BaSi_2$ film heating mechanism. Considering that both silicon and glass covers are transparent to the heater emitted NIR radiant flux (1–1.6 $\mu$m), most of the radiant flux can pass through the cover, and then be absorbed by the $BaSi_2$ film, which is similar to that in $BaSi_2$-E. This implies the low radiative thermal resistance of Si ($R_{\text{rad,Si}}$) and glass ($R_{\text{rad,glass}}$). As shown in Figs. 4(d) and 4(e), the covers also hold the conductive thermal resistance $R_{\text{cond,Si}}$, and $R_{\text{cond,glass}}$, which can be determined by [43]

$$R_{\text{cond}} = d/(k_c A), \tag{2}$$

where $d$ is the thickness of the layer, $k_c$ is the thermal conductivity (a material property), and $A$ is the area normal to the heat flow. The thermal conductivity of Si ($k_{c,Si} = 0.4\,\text{W cm}^{-1}\,\text{K}^{-1}$, when $T > 800\,\text{K}$) is much larger than that of glass ($k_{c,glass} = 0.0142\,\text{W cm}^{-1}\,\text{K}^{-1}$, when $T = 773\,\text{K}$) [44,45]. Their conduction resistances are $R_{\text{cond,Si}} = 0.01\,\text{K W}^{-1}$, and $R_{\text{cond,glass}} = 0.657\,\text{K W}^{-1}$, respectively. The significantly lower conduction resistance of the Si cover enhances its conductive heat transfer as compared to the case of the glass cover. Note that most radiant flux is absorbed by the $BaSi_2$ film; the temperature of the film surface ($T_{\text{film,top}}$) is assumed to be higher than the cover temperature. Heat can be transferred from the film to the cover through thermal conduction. The lower thermal resistance of the Si cover would promote this conductive heat transfer, and decrease the temperature of the film. On the contrary, the high thermal resistance of glass can preserve the heat in the $BaSi_2$ film. This leads to a higher film temperature of $BaSi_2$-G than that of $BaSi_2$-S.

The situation of $BaSi_2$-B is more complicated, due to the absorption of the amorphous $BaSi_2$ layer in the cover. To describe this radiative heat transfer through the $BaSi_2$ layer, the Rosseland approximation of RTE can be used [46,47], given that amorphous $BaSi_2$ is optically thick in the NIR range [20]. The equivalent radiative thermal conductivity ($k_{\text{r}}$) is introduced, which is defined as [48]

$$k_{\text{r}} = \frac{16n^2\sigma}{3\alpha_{\text{R}}}T^3, \tag{3}$$

where $n$ is the refractive index of the medium, $\sigma$ is the Stefan-Boltzmann constant, $T$ is the temperature in K, and $\alpha_{\text{R}}$ is the Rosseland mean absorption coefficient, which is essentially a weighted average of the measured absorption coefficient with the weighting function of the temperature derivative of the Planck emission function [48]. The decrease of the absorption results in the increase of $k_{\text{r}}$, suggesting the lower radiative thermal resistance (e.g., Si and glass). It needs to be mentioned that the quantitative analysis through Eq. (3) is not applicable for Si and glass, as they are transparent at the heater peak-radiation window.

The effective thermal ($k_{\text{eff}}$) conductivity is given by

$$k_{\text{eff}} = k_{\text{c}} + k_{\text{r}}, \tag{4}$$

and the total thermal resistance can be expressed as

$$R_{\text{th, BaSi}_2} = d/(k_{\text{eff}} A), \tag{5}$$

which is illustrated by the parallel thermal resistances $R_{\text{cond}}$ $BaSi_2$, and $R_{\text{rad}}$, $BaSi_2$ in Fig. 4(f). As the thermal parameters of amorphous $BaSi_2$ are unavailable, we can only give a qualitative analysis.

The $BaSi_2$ layer in the cover absorbs the radiant flux resulting in its temperature increase ($T_{\text{mid}}$). The higher temperature of the $BaSi_2$ layer allows the conductive heat transfer to the deep bottom layer and the $BaSi_2$ film. The crystallization of the $BaSi_2$ cover decreases its metallic phase concentration, which, in turn, decreases its absorption in the NIR window. This leads to the increase of radiative thermal conductivity ($k_{\text{r}}$) according to Eq. (3). More heat propagates through the cover by radiation and arrives at the film surface. The $BaSi_2$ film then is heated the same as in the cases of other samples. Here, both conduction and radiation contribute to the crystallization of the film, which is different from other cases, and the cover is speculated to hold a higher temperature as compared to the film at the early phase of annealing. After the full crystallization of the $BaSi_2$ cover and the efficient heat conduction through the glass substrate, the film temperature can be similar or even higher as compared to the $BaSi_2$ cover. The glass in the cover functions the same as the glass cover in $BaSi_2$-G, decreasing the heat conduction through the cover.

Based on the analysis of the thermal resistance network, we can conclude that the $BaSi_2$ film temperature during the annealing is in the order of $BaSi_2$-E > $BaSi_2$-G > $BaSi_2$-B > $BaSi_2$-S. This is in agreement with the absorptance tail in Fig. 3(c). The lower temperature may decrease the degree of the film crystallization and results in a higher concentration of metallic phases within the film [20], which causes the absorptance tail in Fig. 3(c). These metallic phases may also contribute to the increase of the free carrier concentration in Fig. 3(b). Although the film temperatures decrease in FTFA

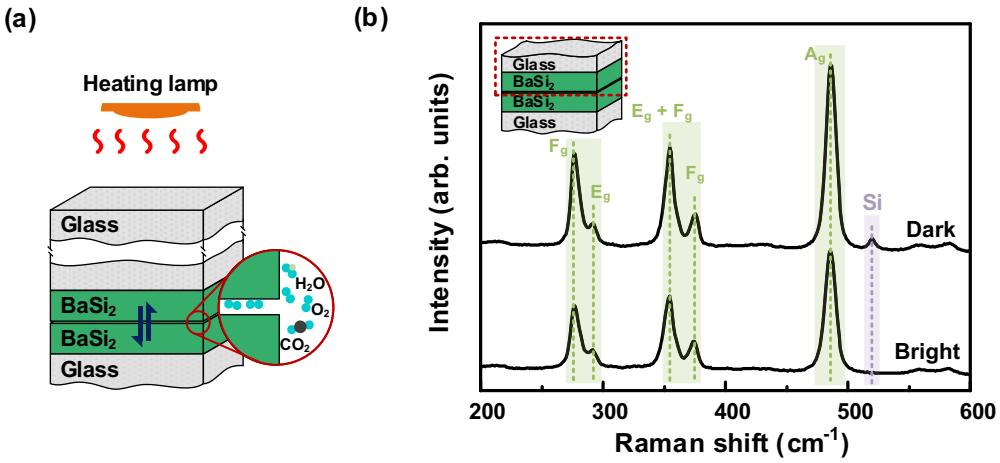


FIG. 5. (a) Schematic illustration of interaction at the interface between the cover and the film. (b) Raman spectra collected from the surface of the BaSi2 cover

samples, the introduction of the cover in the FTFA can contribute to the formation of their homogeneous surfaces. The lateral thermal conduction in the cover can lead to the heat redistribution at the film surface, especially with Si and $BaSi_2$ covers that hold the higher thermal conductivities, enabling a uniformly surface heating process. Meanwhile, the existence of the cover can slow down the film surface temperature decrease during the cooling process due to their higher thermal resistance as compared to the exposed sample ($BaSi_2$-E), which is also beneficial for stress relief of the films.

### 2. *Interactions in the confined space*

Besides the influence on the heat transfer during the annealing and cooling processes, placing the cover on the film provides a confined surface that hinders the gaseous diffusion of residual oxidants in the annealing ambient, for instance, $O_2$, $H_2O$, and $CO_2$, toward the $BaSi_2$ sample surface, and it suppresses the surface oxidation. These residual oxidants in the vacuum ambient lead to the surface oxidation on $BaSi_2$-E, of which the oxide layer can be up to 100 nm thick [25,26]. Consequently, the inhomogeneous surface is formed after annealing. The suppression of surface oxidation benefits the surface homogeneity of FTFA samples.

Besides, the solid-phase and solid-gas reactions within the confined space also play an important role in the FTFA. We first look into the most complicated case, $BaSi_2$-B. The $BaSi_2$ cover shows a higher reactivity at high temperatures compared to Si and glass covers. In the early stage of annealing, the $BaSi_2$ cover exhibits a higher temperature than that of the $BaSi_2$ film. Consequently, the residual oxidants are inclined to react with the $BaSi_2$ cover, as illustrated in Fig. 5(a), including the following reactions [20]:

$$2BaSi_2 + 5O_2 \rightarrow 2BaO + 4SiO_2, \quad (6)$$

$$2BaSi_2 + 2Co_2 + 3O_2 \rightarrow 2BaCO_3 + 4SiO_2, \quad (7)$$

$$BaSi_2 + 5H_2O \rightarrow BaO + 2SiO_2 + 5H_2(g), \quad (8)$$

$$2BaSi_2 + SiO_2 \rightarrow 2BaO + 5Si. \quad (9)$$

Surface oxidation of $BaSi_2$ can be attributed to Eqs. (6)–(8), while the formation of Si NCs is the outcome of the reaction between $BaSi_2$ and oxide demonstrated by Eq. (9). The $BaSi_2$ cover functions as the sacrificial protection layer consuming the oxidants within the confined space. This is proved by the formation of Si NCs at the $BaSi_2$ cover surface. The $BaSi_2$ cover demonstrates an inhomogeneous surface with dark and bright areas, as shown in Fig. S4 in the Supplemental Material [39]. A weak Raman peak of Si NCs at $\sim 519\,cm^{-1}$ can be observed in the spectrum of the dark area, as shown in Fig. 5(b). Meanwhile, more cracks can be noticed at the surface of the $BaSi_2$ cover than at that of $BaSi_2$ films, suggesting the nonuniform heat distribution within the cover. This can be ascribed to the surface oxidation and cover surface roughness that alters the radiant flux absorption.

No obvious change can be noticed at the surface of the Si and glass cover, whose temperatures are lower than that of the $BaSi_2$ cover. Among them, the Si cover may consume part of the oxidants, while the glass cannot decrease the oxidant content. Meanwhile, the rather smooth surface of the glass and silicon wafer can reduce the volume of the confined space as well as the content of oxidants. Hence, we can speculate that the $BaSi_2$ film surface oxidation degree, from severe to mild, is in the order of $BaSi_2$-E $\gg$ $BaSi_2$-G $>$ $BaSi_2$-S $\approx$ $BaSi_2$-B. The suppression of surface oxidation also alleviates the Fe accumulation at the surface layer and the formation of $FeSi_2$ in the FTFA samples.

In addition, the atomic interdiffusion may also occur during the FTFA, similar to the case of GaAs [27]. Our previous research has revealed the phenomenon of elemental interdiffusion between $BaSi_2$ and substrates ($SiO_x$ and Si) [20,26]. Given the lower temperature of the glass cover, we may assume that limited interdiffusion, majorly Ba diffusion into the glass, occurs at the glass/$BaSi_2$ interface in $BaSi_2$-G [20]. Si and Ba interdiffusions can occur instead at the interface of Si/$BaSi_2$ in the $BaSi_2$-S. Movements of Si into $BaSi_2$ film and Ba into the Si cover can result in a Si-rich composition at the $BaSi_2$ film surface, which can improve its crystallinity [41,49]. The interdiffusion at the $BaSi_2$/$BaSi_2$ interface in $BaSi_2$-S is hard to predict; various diffusions may happen due to their high reactivities and higher temperatures.

Owing to the severe surface oxidation, $BaSi_2$-E shows the worst surface crystallinity. The suppression of the oxidation improves the surface crystallinity of the FTFA samples. Additionally, the interdiffusion at the cover/$BaSi_2$ interface (especially in $BaSi_2$-S and $BaSi_2$-B) may further improve their film surface quality. These results are also in good agreement with the position shift of the $A_g$ Raman peak presented in Fig. 3(a).

The oxidation and interdiffusion at the confined space at the cover/$BaSi_2$ interface (i) significantly alter the properties of the $BaSi_2$ surface, including surface homogeneity, composition, and crystallinity; (ii) may influence the longitudinal elemental diffusion within the film, which may affect other properties of the film, such as the conduction type and carrier concentration as shown in Fig. 3(b). However, further investigations on bulk properties as well as the optimizations on FTFA parameters, such as temperature, duration, broad-range cover materials, heating source (emission wavelength), etc., are needed for a comprehensive understanding of the FTFA mechanism and its effects on $BaSi_2$ films.

## IV. CONCLUSION

The FTFA approach, with various covers including $BaSi_2$, Si, and glass, is introduced in the postgrowth treatment of sputtered $BaSi_2$ films for the material crystallization and thin-film properties improvement from perspectives of surface homogeneity and crystal quality. Impacts of FTFA on sputtered $BaSi_2$ film properties majorly originate from two aspects: (i) the employment of the covers in the FTFA alters the heating mechanism of the film from radiation to a combination of radiation and conduction, which results in the lateral and longitudinal heat redistribution within the sample and covers; (ii) the confined space produced by the covers and the film grants lower-content residual gaseous oxidants at the film surface and causes the elemental interdiffusions between the cover and the film, which tailors the film surface properties. These thermal processes and interfacial interactions coordinatively determine the film properties. Optimizations of the FTFA method, including temperature, duration, cover materials, heating source, ambient, etc., are needed for the further improvement and control of the $BaSi_2$ film properties.

## ACKNOWLEDGMENTS

The authors would like to thank Martijn Tijssen for daily technical equipment support. Y.T. acknowledges financial support from the China Scholarship Council (Grant No. 201606320243).

[1] K. Toh, T. Saito, and T. Suemasu, Jpn. J. Appl. Phys. **50**, 068001 (2011).
[2] T. Suemasu and N. Usami, J. Phys. D: Appl. Phys. **50**, 023001 (2016).
[3] W. Du, R. Takabe, S. Yachi, K. Toko, and T. Suemasu, Thin Solid Films **629**, 17 (2017).
[4] K. O. Hara, N. Usami, K. Nakamura, R. Takabe, M. Baba, K. Toko, and T. Suemasu, Appl. Phys. Express **6**, 112302 (2013).
[5] R. Takabe, K. O. Hara, M. Baba, W. Du, N. Shimada, K. Toko, N. Usami, and T. Suemasu, J. Appl. Phys. **115**, 193510 (2014).
[6] T. Deng, T. Suemasu, D. A. Shohonov, I. S. Samusevich, A. B. Filonov, D. B. Migas, and V. E. Borisenko, Thin Solid Films **661**, 7 (2018).
[7] R. Du, K. Yang, X. Gao, W. Shi, W. Du, Y. Zhang, and T. Suemasu, Mater. Lett. **260**, 126936 (2020).
[8] K. O. Hara, Y. Nakagawa, T. Suemasu, and N. Usami, Jpn. J. Appl. Phys. **54**, 07JE02 (2015).
[9] N. A. A. Latiff, T. Yoneyama, T. Shibutami, K. Matsumaru, K. Toko, and T. Suemasu, Phys. Status Solidi C **10**, 1759 (2013).
[10] T. Yoneyama, A. Okada, M. Suzuno, T. Shibutami, K. Matsumaru, N. Saito, N. Yoshizawa, K. Toko, and T. Suemasu, Thin Solid Films **534**, 116 (2013).
[11] Y. Inomata, T. Nakamura, T. Suemasu, and F. Hasegawa, Jpn. J. Appl. Phys. **43**, L478 (2004).
[12] M. Kobayashi, Y. Matsumoto, Y. Ichikawa, D. Tsukada, and T. Suemasu, Appl. Phys. Express **1**, 051403 (2008).
[13] T. Suemasu, Jpn. J. Appl. Phys. **54**, 07JA01 (2015).
[14] Q. Deng, H. Chen, H. Liao, L. Chen, G. Wang, S. Wang, and Y. Shen, J. Phys. D: Appl. Phys. **52**, 075501 (2018).
[15] J.-S. Huang, K.-W. Lee, and Y.-H. Tseng, J. Nanomater. **2014**, 238291 (2014).
[16] S. Yachi, R. Takabe, H. Takeuchi, K. Toko, and T. Suemasu, Appl. Phys. Lett. **109**, 072103 (2016).
[17] K. Kodama, R. Takabe, T. Deng, K. Toko, and T. Suemasu, Jpn. J. Appl. Phys. **57**, 050310 (2018).
[18] K. O. Hara, N. Usami, Y. Hoshi, Y. Shiraki, M. Suzuno, K. Toko, and T. Suemasu, Jpn. J. Appl. Phys. **50**, 08LB03 (2011).
[19] K. O. Hara, K. Arimoto, J. Yamanaka, and K. Nakagawa, J. Mater. Res. **33**, 2297 (2018).
[20] Y. Tian, R. Vismara, S. Van Doorene, P. šutta, Ľ. Vančo, M. Veselý, P. Vogrinčič, O. Isabella, and M. Zeman, ACS Appl. Energy Mater. **1**, 3267 (2018).
[21] K. O. Hara, Y. Hoshi, N. Usami, Y. Shiraki, K. Nakamura, K. Toko, and T. Suemasu, Thin Solid Films **557**, 90 (2014).
[22] M. A. Khan, M. Takeishi, Y. Matsumoto, T. Saito, and T. Suemasu, Phys. Procedia **11**, 11 (2011).
[23] M. Takeishi, Y. Matsumoto, R. Sasaki, T. Saito, and T. Suemasu, Phys. Procedia **11**, 27 (2011).
[24] K. O. Hara, Y. Hoshi, N. Usami, Y. Shiraki, K. Nakamura, K. Toko, and T. Suemasu, Thin Solid Films **534**, 470 (2013).
[25] Y. Tian, A. R. Montes, Ľ. Vančo, O. Isabella, and M. Zeman, Jpn. J. Appl. Phys. **59**, SFFA03 (2020).
[26] Y. Tian, A. R. Bento Montes, Ľ. Vančo, M. Čaplovičová, P. Vogrinčič, P. Šutta, L. Satrapinskyy, M. Zeman, and O. Isabella, Adv. Mater. Interfaces **7**, 2000887 (2020).
[27] H. Kanber, R. J. Cipolli, W. B. Henderson, and J. M. Whelan, J. Appl. Phys. **57**, 4732 (1985).
[28] G. Nam, Y. Park, I. Ji, B. Kim, S.-H. Lee, D. Y. Kim, S. Kim, S.-O. Kim, and J.-Y. Leem, ACS Appl. Mater. Interfaces **7**, 873 (2015).
[29] H. Miyake, C.-H. Lin, K. Tokoro, and K. Hiramatsu, J. Cryst. Growth **456**, 155 (2016).

[30] J. Wang, W. Li, H. Zhang, Y. Xiong, L. Ye, H. Ruan, G. Qin, and C. Kong, Appl. Phys. A **126**, 235 (2020).
[31] Y. Kimura, M. Fujiwara, Y. Nakagawa, K. Gotoh, Y. Kurokawa, and N. Usami, Jpn. J. Appl. Phys. **59**, SFFA05 (2020).
[32] T. Suhara, K. Murata, A. Navabi, K. O. Hara, Y. Nakagawa, C. T. Trinh, Y. Kurokawa, T. Suemasu, K. L. Wang, and N. Usami, Jpn. J. Appl. Phys. **56**, 05DB05 (2017).
[33] M. Somer, Z. Anorg. Allg. Chem. **626**, 2478 (2000).
[34] A. G. Birdwell, R. Glosser, D. N. Leong, and K. P. Homewood, J. Appl. Phys. **89**, 965 (2001).
[35] T. Yoshitake, T. Nagamoto, and K. Nagayama, Thin Solid Films **381**, 236 (2001).
[36] G. Faraci, S. Gibilisco, P. Russo, A. R. Pennisi, and S. La Rosa, Phys. Rev. B **73**, 033307 (2006).
[37] S. Matsuno, R. Takabe, S. Yokoyama, K. Toko, M. Mesuda, H. Kuramochi, and T. Suemasu, Appl. Phys. Express **11**, 071401 (2018).
[38] K. O. Hara, C. T. Trinh, Y. Kurokawa, K. Arimoto, J. Yamanaka, K. Nakagawa, and N. Usami, Jpn. J. Appl. Phys. **56**, 04CS07 (2017).
[39] See Supplemental Material at http://link.aps.org/supplemental/10.1103/PhysRevMaterials.4.125403 for optical microscopy images, Raman peak information, film resistivity results, and optical properties.
[40] H. Peng, C. Wang, J. Li, R. Zhang, M. Wang, H. Wang, Y. Sun, and M. Sheng, Phys. Lett. A **374**, 3797 (2010).
[41] R. Takabe, T. Deng, K. Kodama, Y. Yamashita, T. Sato, K. Toko, and T. Suemasu, J. Appl. Phys. **123**, 045703 (2018).
[42] M. F. Modest, *Radiative Heat Transfer* (Academic Press, New York, 2013).
[43] F. Kreith, R. M. Manglik, and M. S. Bohn, *Principles of Heat Transfer* (Cengage Learning, Boston, 2012).
[44] H. R. Shanks, P. D. Maycock, P. H. Sidles, and G. C. Danielson, Phys. Rev. **130**, 1743 (1963).
[45] Corning EAGLE Slim Glass, https://www.corning.com/worldwide/en/products/display-glass/products/eagle-xg-slim.html.
[46] E. Magyari and A. Pantokratoras, Int. Commun. Heat Mass Transfer **38**, 554 (2011).
[47] S. Rosseland, *Astrophysik: Auf Atomtheoretischer Grundlage* (Springer-Verlag, Berlin, 2013), Vol. 11.
[48] H. Keppler, L. S. Dubrovinsky, O. Narygina, and I. Kantor, Science **322**, 1529 (2008).
[49] Y. Yamashita, Y. Takahara, T. Sato, K. Toko, A. Uedono, and T. Suemasu, Appl. Phys. Express **12**, 055506 (2019).